Additive Manufacturing Letters 11 (2024) 100234

Contents lists available at ScienceDirect

Additive Manufacturing Letters

journal homepage: www.elsevier.com/locate/addlet

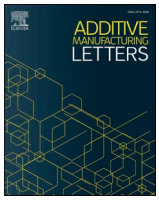

Short Communication

High-temperature tensile behaviors of an ultra-strong aluminum alloy fabricated by additive manufacturing

Anyu Shang, Benjamin Stegman, Xuanyu Sheng, Ke Xu, Yifan Zhang, Chao Shen, Emiliano Flores, Tanner McElroy, Haiyan Wang, Xinghang Zhang *

School of Materials Engineering, Purdue University, West Lafayette, IN, 47907, USA

ARTICLE INFO

Keywords:
Aluminum alloys
Laser deposition
Tension test
High-temperature deformation
Intermetallics

ABSTRACT

Additively manufactured (AM) Al alloys have widespread applications. Their high-temperature mechanical behaviors are also of significant interest. In this study, we investigated the microstructure and mechanical behavior of Al-2Ti-2Fe-2Co-2Ni (at%) alloy processed by laser powder bed fusion. The as-printed alloy contains a distinctive heterogeneous microstructure characterized by nanoscale intermetallic lamellae arranged in rosette patterns in the Al matrix. Notably, this alloy exhibits high tensile strength and thermal stability up to 500 °C as revealed by in-situ tension studies in a scanning electron microscope. The enhanced high temperature performance can be attributed to a substantial volume fraction of well-dispersed, nanoscale stable intermetallic particles.

1. Introduction

Aluminum alloys found wide applications in aerospace, marine and automobile industries due to their high specific strength, excellent oxidation resistance and low cost. To fulfill the needs of geometrical flexibility, laser powder bed fusion was developed to additively manufacture Al alloy parts, where laser selectively fuses the region of interest on each thin layer of powder and the geometry is dictated by layer-wise construction. However, high-strength Al alloys, such as 2xxx and 7xxx series, generally suffer from printing defects, with hot tearing being the most catastrophic damage [1–8]. Besides, these commercial Al alloys soften significantly at elevated temperatures ranging from 200 to 450 °C due to the degradation or dissolution of strengthening precipitates [9–11]. High-strength, lightweight, thermally stable Al alloys operated at elevated temperatures are in high demand.

Transition metals can form multiple intermetallics phases that are typically stable and resistant to coarsening due to their low mobility and large formation energy in Al matrix [10]. With the inherent nature of rapid solidification, laser powder bed fusion is capable of refining and dispersing intermetallics that tend to overgrow in traditional metallurgy. This rapid quenching characteristic opens an opportunity for AM Al alloy development, evidenced by Al-Fe [12–15], Al-Ni [16], Al-Fe-Ni [17,18], Al-Fe-Cr [19,20], and Al-Cu [21,22]. Intermetallic-forming rare-earth elements also serves the same purpose as proven in Al-Ce [23–26], Al-Zr-Sc [27,28]. However, alloys with near-eutectic compositions are generally preferred as they have better printability due to a smaller freezing range countering cracking at the expense of mechanical strength [1,29–31]. In this study, striving to maximize precipitate strengthening and thermal stability from incorporating transition metals, a customized Al alloy with the composition Al-2Ti-2Fe-2Co-2Ni (at%) was manufactured. The as-printed alloys exhibit a heterogeneous distribution of lamellar intermetallic colonies in Al matrix, rendering its combination of strength and deformability under compression, as reported previously [32,33]. Herein, we investigated its microstructural evolution and mechanical behaviors at elevated temperatures under tension. This alloy shows exceptional thermal stability and strength with limited tensile ductility at high temperatures.

2. Materials and methods

The pre-alloyed powder with a nominal composition of Al-2Ti-2Fe-2Co-2Ni (at%) was gas-atomized satisfying −53+15 μm by Atlantic Equipment Engineering, Inc. The powder was utilized for laser powder bed fusion in an SLM 125 HL printer on build plates that were preheated to 200 °C. The chamber was flushed with ultra-high-purity Argon and afterwards the oxygen partial pressure was controlled to be < 0.10% during the process. Additive manufacturing was performed by using an IPG laser with a wavelength of 1070 nm, a laser power of 200 W, a laser

* Corresponding author.
E-mail address: xzhang98@purdue.edu (X. Zhang).

https://doi.org/10.1016/j.addlet.2024.100234
Received 15 May 2024; Received in revised form 3 August 2024; Accepted 17 August 2024
Available online 17 August 2024

spot diameter of 70 μm, a scan speed of 1200 mm/s, a hatch spacing of 100 μm, a layer thickness of 30 μm and a layer rotation of 67° Thin flat coupons with dimensions 2 × 8 × 35 (height) mm were vertically printed upon a 3-mm thick scaffold support structure (Fig. 1a). After parts were sectioned off the plates by wire electrical discharge machining, tensile specimens were engraved from flat coupons. As for the heat treatment, as-printed bars were put into a muffle furnace after the targeted temperature was reached. After a certain period of annealing, samples were quenched in water. Samples were grinded and polished down to 1 μm diamond paste, then characterized by scanning electron microscopy (SEM) on a Thermo Fisher Teneohigh-resolution Field Emission scanning electron microscope operated at 20 kV with a back-scattered detector. XRD spectrums were collected on a PANalytical Empyrean X'pert PRO MRD diffractometer with a 2 × Ge (220) hybrid monochromator to select Cu $K_{\alpha 1}$ in the 2θ-ω geometrical configuration. Vickers hardness tests utilized a load of 100 gf and a holding time of 10 s. Microhardness values were averaged from 20 measurements. Tension tests were performed inside TeneoSEM microscope using a Kammrath-Weiss in-situ tensile frame at a strain rate of 10^{-3} s^{-1} using a 10 kN load cell at room and elevated temperatures. Each tension specimen was heated with the heating stage and soaked at the designated temperature for 30 min before testing to assure temperature accuracy. Focused ion beam was utilized to lift out thin lamellae with the final cleaning voltage 2 kV and current 44 pA, respectively. Transmission electron microscopy (TEM), scanning transmission electron microscopy (STEM) and Energy dispersive spectrometry (EDS) mapping were conducted on a Thermo Fisher Talos 200X transmission electron microscope with an acceleration voltage of 200 kV.

3. Results and discussion

3.1. Microstructure in the as-printed state

Additively manufactured Al-2Ti-2Fe-2Co-2Ni (at%) Al alloy presents a heterogeneous microstructure with inter-woven laser track seen on the cross section (Fig. 1b) in the as-printed state. A high magnification back-scattered SEM micrograph reveals distinctive morphologies across melt pool boundaries (Fig. 1c), namely, coarse rosette regions and fine rosette regions. The non-uniformity could result from variation of solidification rate and temperature gradient inside melt pools. Both regions feature radially arranged nanoscale intermetallic lamellae forming so-called "rosettes", whereas fine rosettes have thinner lamellae thickness (t = 80 nm) than coarse rosettes (t = 200 nm) due to a higher quench rate. In addition, coarse rosette regions contain eutectic intermetallics in Al matrix (dark contrast) on the periphery of coarse rosettes, and dominate melt pool interior (Fig. 1d), while fine rosette regions tend to reside near the bottom of melt pools with tightly packed fine rosettes and have less content of Al (Fig. 1e). Colony size of rosettes are around 1.5 μm in diameter, and comparable for both regions.

The subtle microstructures of fine rosettes are shown in Fig. 2a in TEM. Along with XRD spectrums in Fig. S1, EDS maps demonstrate these rosettes contain a cruciform Al_3Ti core and surrounding alternate lamellae composed of Al_3Ti and $Al_9(Fe,Co,Ni)_2$. The line scan across intermetallic platelets confirms the pure intermetallic nature of the rosettes (Fig. 2b). Similar constituents could be found in coarse rosettes, but with larger dimensions (Fig. S2). The hierarchical aggregation of intermetallics reflect complex precipitation behaviors. Primary Al_3Ti forms initially due to its higher melting temperature, serving as easy nucleation sites for co-precipitation of two intermetallics. Al matrix solidifies in the end and cellular $Al_9(Fe,Co,Ni)_2$ form because of decreasing solubility as temperature drops.

3.2. Thermal stability

To assess the microstructural stability, isothermal annealing for 2 h up to 600 °C were performed on the Al-2Ti-2Fe-2Co-2Ni (at%) alloy and its microhardness was documented in Fig. 3a. The large volume fraction of intermetallics led to a high microhardness value ~ 200 HV (2.0 GPa) in the as-printed state. In fact, intermetallic volume fraction can reach 45% on average (with the lever rule calculated from compositions in Figs. 2b and S2b). Post-annealing samples manifest a gradual decrease in hardness to ~ 150 HV (1.5 GPa) as treatment temperature increased to

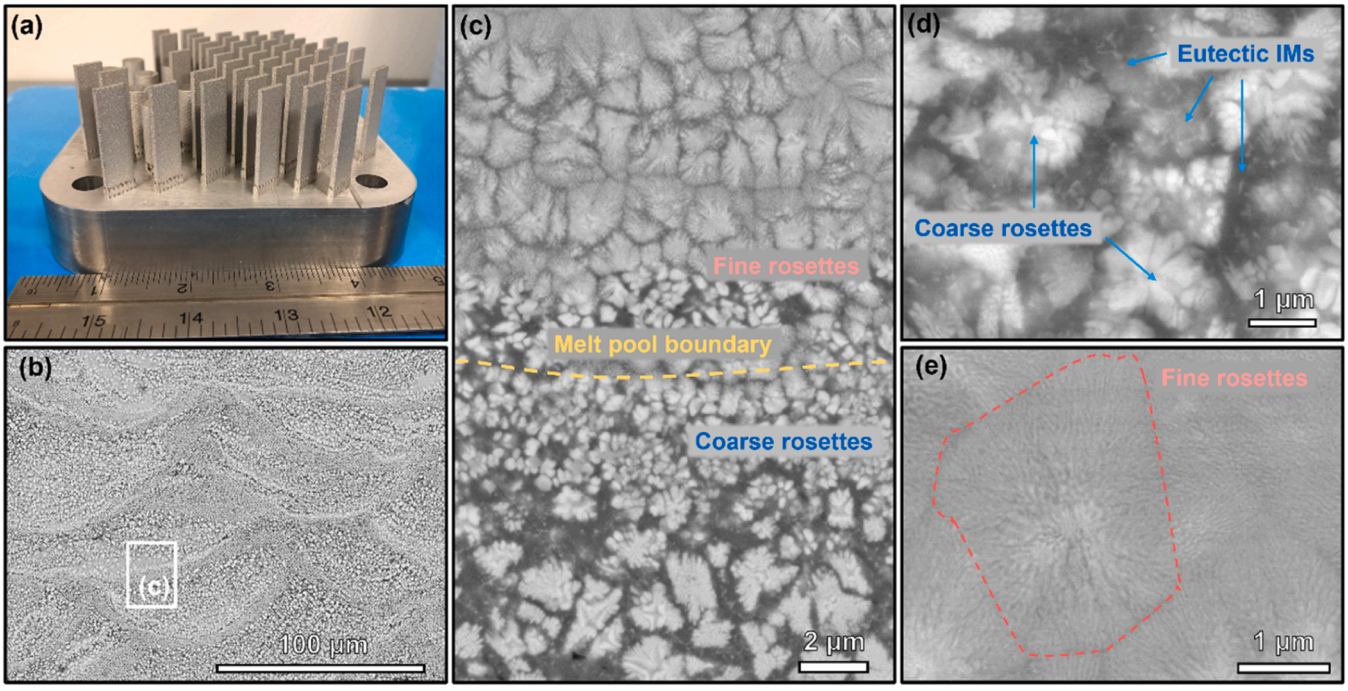

Fig. 1. (a) An optical image of the as-printed Al-2Ti-2Fe-2Co-2Ni (at%) alloy tensile bars (Ruler in inches). (b) An overview of multiple laser melt pool layers in the Al alloys. (c) An SEM micrograph showing the heterogeneous microstructure across melt pool boundaries. (d, e) Higher magnification SEM micrographs showing coarse rosettes and fine rosettes, respectively.

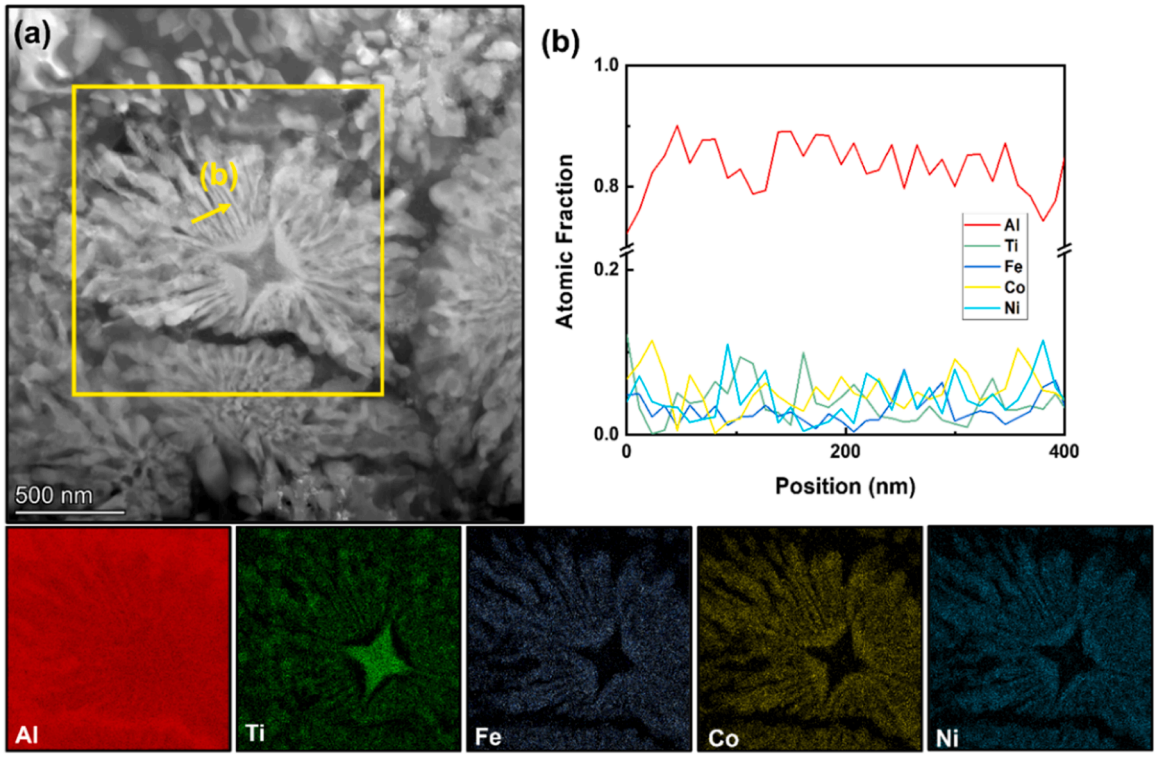

Fig. 2. (a) A STEM micrograph on the fine rosettes in the as-printed alloy. Elemental distribution maps were shown below for the region denoted by the yellow square. (b) An EDS line scan revealing atomic fractions following the yellow arrow in (a).

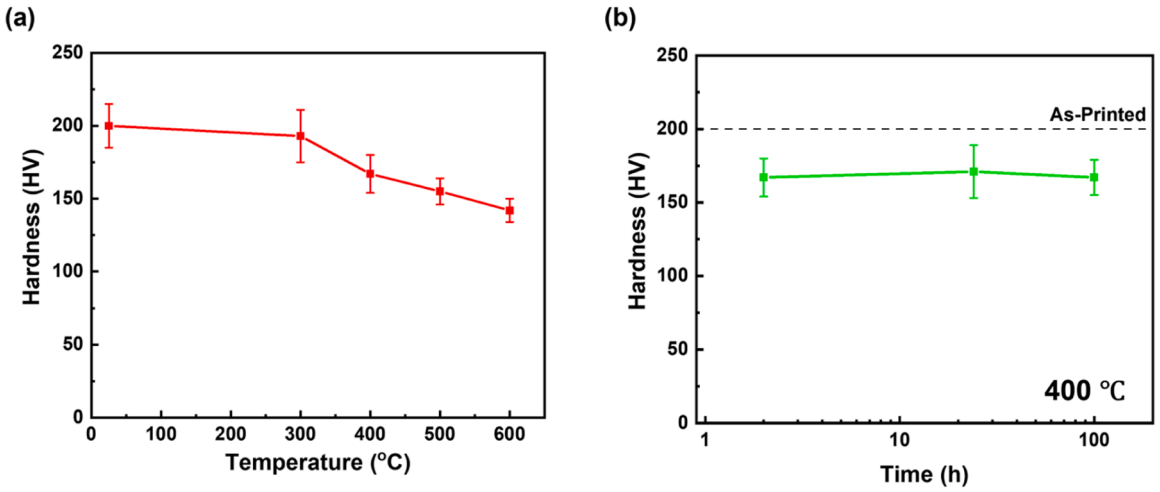

Fig. 3. (a) The microhardness for the current alloy after a 2-hour annealing process. (b) The evolution of hardness after isothermal annealing at 400 °C.

600 °C ($T = 0.93\ T_m$ of Al matrix). The largely preserved high hardness at this extreme temperature indicates a significant resistance of the alloy to thermal degradation. Furthermore, the evolution of hardness was captured in Fig. 3b after isothermal annealing at 400 °C. Vickers hardness value reached 170 HV after the initial 2-hour exposure and no obvious softening was recorded even after 100 h of heat treatment, which provided the evidence of excellent thermal stability of the AM Al alloy at 400 °C.

Microstructure evolutions on coarse and fine rosette regions after the aforementioned thermal exposure were revealed by SEM micrographs in Fig. 4. Compared with the as-printed state, annealing at 300 °C did not alter the microstructure for both regions (Fig. 4a–c), which was corroborated by the minor microhardness reduction in Fig. 3a. When the annealing temperature increased further to 400 °C, fine rosettes underwent moderate ripening while the coarsen rosettes remained unchanged (Fig. 4d–f). Extending the duration to 100 h did not yield prominent ripening in both regions, but some intermetallics nanolaminates in the fine rosettes appeared to spheroidize (Fig. 4g–i), i.e., the layered nano-lamellae were decomposed into discrete globular precipitates (Fig. 4i). At 500 °C, both regions showed prominent coarsening. In this condition, coarse rosettes coarsened into relatively larger, cruciform precipitate aggregates, whereas fine rosettes evolved into larger, discontinuous precipitates by spheroidization mechanism (Fig. 4j–l). It is worth mentioning that globular precipitates became faceted with preferred orientations or crystallographic planes. The microstructure with periodic alternation of coarse and fine rosettes was not homogenized until the specimen was heated up to 600 °C (Fig. 4m). Dense intermetallic lamellae were replaced with micron- or submicron-

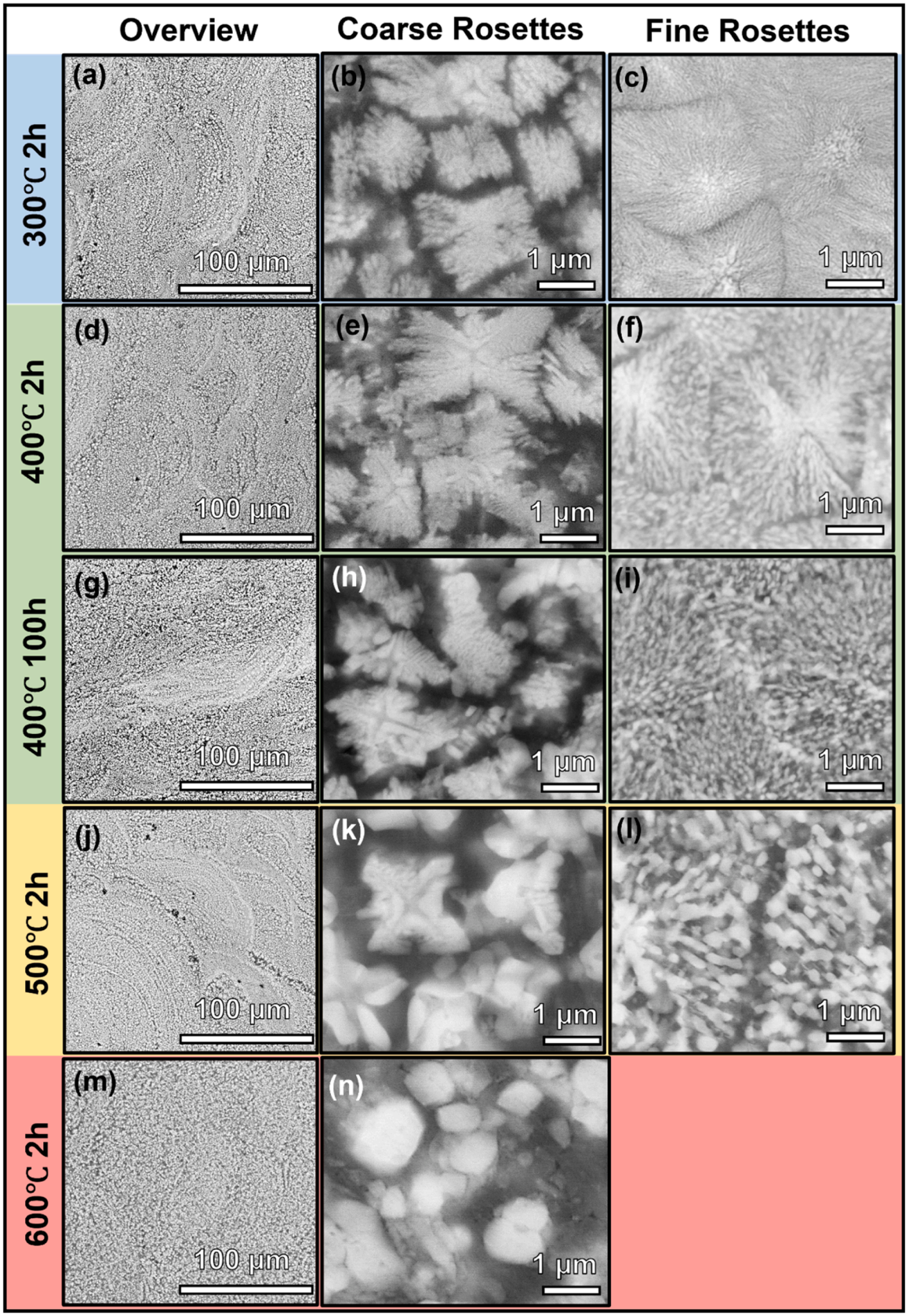

Fig. 4. Back-scattered SEM micrographs revealing the microstructure evolution after annealing at different temperatures for regions with coarse rosettes and fine rosettes. (a, b, c) 300 °C, 2 h; (d, e, f) 400 °C, 2 h; (g, h, i) 400 °C, 100 h; (j, k, l) 500 °C, 2 h; (m, n) 600 °C, 2 h.

sized individual globular particles dispersed in the Al matrix (Fig. 4n).

TEM characterizations acquired for the sample annealed at 400 °C for 100 h are presented in Fig. 5 to study the microstructure evolution. As shown in Fig. 5a, spheroidization occurs in the fine rosette region. The magnified TEM micrograph in Fig. 5b shows semi-faceted intermetallic particles. The EDS maps in Fig. 5c manifest the coexistence of Al_3Ti and $Al_9(Fe,Co,Ni)_2$ fine intermetallic particles in Al matrix. Fig. 5d reveals the atomic arrangements along the intermetallic interface. The selected area diffraction pattern (SAED) of rosettes in Fig. 5e shows the orientation relationships between two types of intermetallics are the same as those in the as-printed sample, where $[1\bar{3}0]_{Al_3Ti}$ // $[100]_{Al_9(Fe,Co,Ni)_2}$, $(002)_{Al_3Ti}$ // $(001)_{Al_9(Fe,Co,Ni)_2}$, $(310)_{Al_3Ti}$ // $(010)_{Al_9(Fe,Co,Ni)_2}$ with matched interplanar spacing, $d^{(002)}_{Al_3Ti}$: $d^{(001)}_{Al_9(Fe,\ Co,\ Ni)_2} \approx 1{:}2$ and $d^{(310)}_{Al_3Ti} : d^{(010)}_{Al_9(Fe,Co,Ni)_2} \approx 1{:}5$ [32].

The thermal stability of rosettes warrants further discussion. Lamellar thickness was measured for coarse and fine rosettes after heat treatment. As shown in Fig. 6, increasing annealing temperature leads to a greater lamellar thickness. From the thermodynamics point of view, it is postulated the driving force for rosette coarsening is the minimization of interfacial energy. First, fine rosettes showed coarsening of laminates after 2 h annealing at 400 °C, whereas coarse rosettes did not reveal prominent differences in their laminate thickness after annealing in the same condition (Fig. 4e and f). The difference in thermal stability of fine and coarse rosettes can be rationalized by their difference in excess Gibbs free energy associated with laminate interfaces. Finer microstructures are thermodynamically more unstable, rendering their increasing vulnerability to coarsening during annealing. Second, spheroidization of laminate rosettes was witnessed at 400 °C, which is another phenomenon related to interface curvatures. Further extending

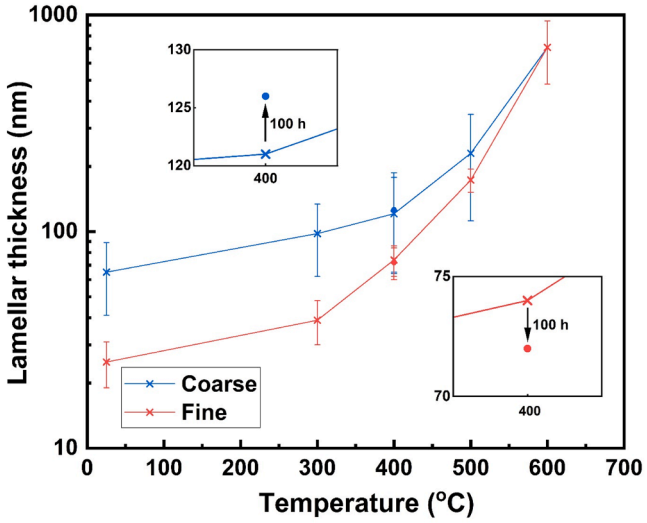

Fig. 6. Evolutions of lamellar thickness for coarse and fine rosettes annealed at elevated temperatures for 2 h (datapoints marked by crosses). The two inserts visualize minute lamellar thickness changes (marked by dots) extending the durations to 100 h.

annealing time to 100 h did not yield prominent dimension changes but slightly more pronounced spheroidization (Figs. 4f and i, 5a and b and 6). Spheroidization was realized by the chemical potential inhomogeneity for precipitates with a given shape [34,35]. The chemical potential fluctuation imposed by capillary force on the convex/concave

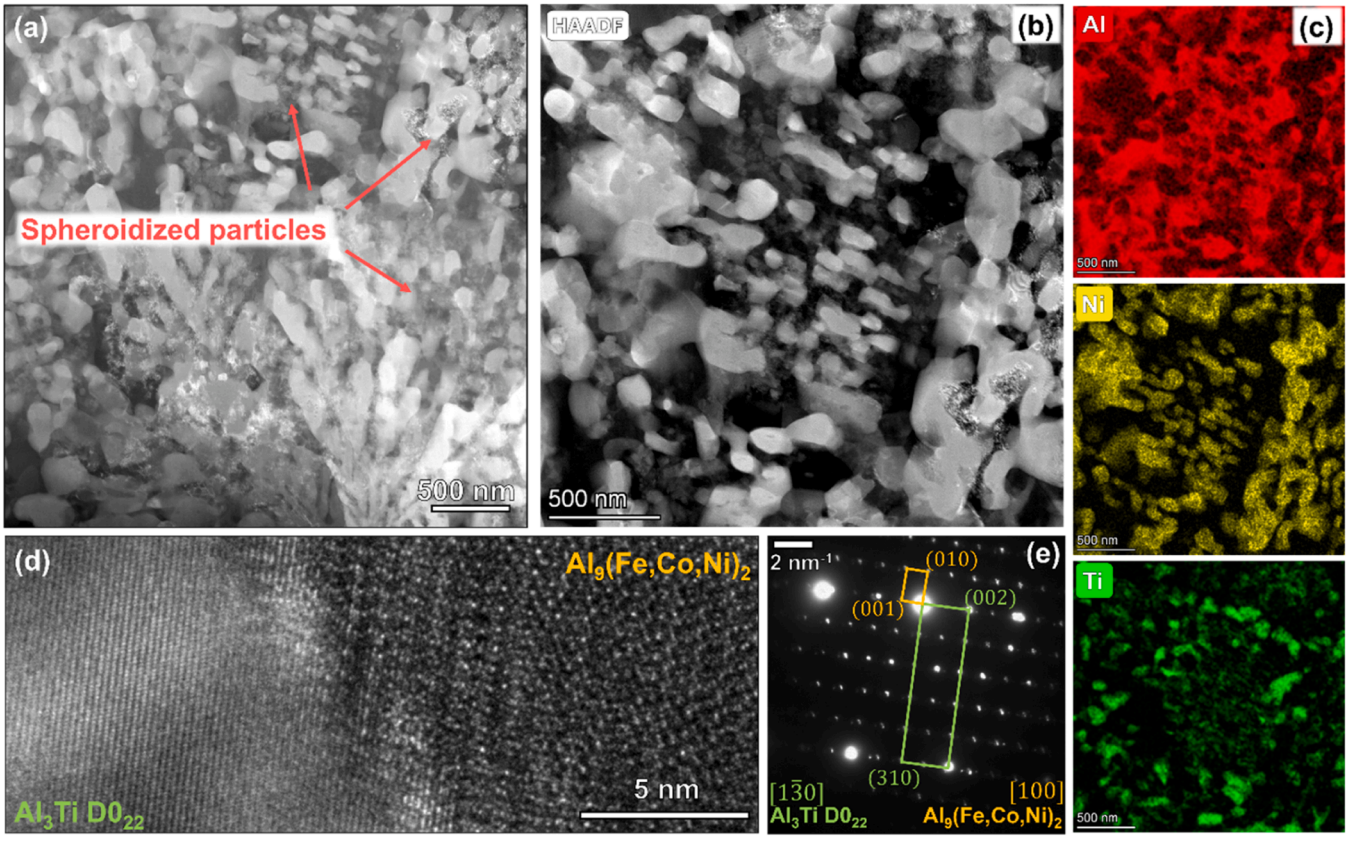

Fig. 5. TEM/STEM characterizations on the sample annealed at 400 °C for 100 h. (a) An overview STEM micrograph revealing the spheroidized particles in the inter-rosette regions. (b) A magnified STEM image showing the detailed morphology of some faceted spheroidized particles with elemental (Al, Ni, Ti) distribution maps in (c). (d) A high-resolution TEM image along the Al_3Ti and $Al_9(Fe,Co,Ni)_2$ intermetallic interface. (e) SAD pattern showing the matched interplanar spacing between the Al_3Ti and $Al_9(Fe,Co,Ni)_2$.

interface initiates local diffusion through dislocation channels or along interfaces. Eventually the interface curvature, hence the chemical potential, is unified and nano-lamellae evolve into globular precipitates. Third, spheroidized precipitates in the fine rosette region were faceted after annealing at 500 °C (Figs. 4l and 5b), which mimics Wulff constructions as a result of minimization of total interfacial energy with a conserved volume [36]. Furthermore, interfaces satisfying certain orientation relationships with matched crystallographic interplanar spacing are more stable (Fig. 5e). Therefore, these low-energy interfaces are favored when enveloping precipitates.

Inferred from microstructural evolution, it could be speculated that excellent thermal stability stem from kinetic and dynamic factors. The breakdown of intermetallic rosettes could lead to gradual softening as annealing temperature increases. The onset of perceivable coarsening for the current alloy started at 400 °C, followed by relatively slow ripening at higher temperatures. The sluggish dynamics is roughly aligned with the literature data for Al-Fe-Ni alloys [17,18,37,38] owing to the minute solubility and low diffusivities of Fe, Co and Ni in Al matrix at intermediate temperatures [10,39]. However, the diffusivities of Fe, Co, Ni approach the self-diffusivity of Al at higher temperatures (400 °C and above), resulting in coarsening [10]. In this case, the addition of the extremely slow diffusor (in Al matrix), Ti, could retard the coarsening [10]. Recently the synergistic effects of solute pairs, such as Fe and Ti, have been observed in sputtered high strength Al-Fe-Ti alloys. Similar synergy effect has been observed in Al-Ni-Ti [40] and Al-Co-Zr [41] alloys. Besides, kinetic factors also play a role. Stable intermetallics have a low tendency for self-dissolution, impeding the supplies of transition metals for diffusion at Al-intermetallics interface.

3.3. Tension tests at elevated temperatures

With the established thermal and microstructural stability, the possibility of the current alloy for high temperature applications was explored. Stress-strain curves of in-situ SEM tensile tests were recorded at various temperatures for the as-fabricated samples (Fig. 7a). It could be seen the tensile behaviors examined at room and elevated temperatures up to 400 °C were similar with a relatively consistent yield stress around 360 MPa, premature fracture and a limited ductility, around 1%. Further increasing the test temperature to 500 °C, the yield stress halved to 170 MPa with 1% plasticity. The high volume fraction of intermetallics (45 vol%) may account for the limited tensile ductility. These data were incorporated into a literature survey on the relationship between yield strength and test temperature in Fig. 7b based on selected cast or LPBF-processed Al alloys [15,25,42–55]. As the test temperature increases, the yield strength of the current alloy stands out, especially at 400 and 500 °C. In the dilemma of strength and ductility, this alloy will roughly depict the upper bound of strength achievable by AM-introduced precipitate strengthening at 300–500 °C. In the meantime, 45 vol% intermetallics seems to embrittle Al at below 400 °C and maintain some plasticity at 500 °C.

Given the complex microstructure involving intermetallic rosettes, their roles in tensile deformation are revealed by fractography analyses for specimens tested at room temperature and 500 °C. Low-magnification SEM micrographs of fracture surfaces show alternate bright and dark contrasts, which roughly correspond to coarse and fine rosette regions, respectively (Fig. 8a and d). It could be seen that the majority of plastic flow took place in Al matrix in the coarse rosette region, indicated by the extruded peripheral ridges in brighter contrast around rosettes (Fig. 8b and e). The coarse rosettes showed cleavage failure due to the brittle nature of the intermetallics. As for the fine rosettes, the fractured surface exhibited a rugged appearance at room temperature, implying a tortuous pathway for crack propagation (Fig. 8c). This sinuous crack morphology suggests fine rosettes can toughen the material because the generation of extra free surface is energetically expensive. Note in fine rosette region there is no prominent Al ridges, which may imply the plastic deformation (if any) was in concert between Al and intermetallic rosettes. Similar phenomenon was observed at 500 °C (Fig. 8f), only that some fine rosettes degraded so that inter-rosette Al partially accommodated deformation.

In addition, there is a discrepancy in the mechanical behaviors for the current alloy under compression [32] and tension (this work). Subject to compression, samples exhibited an ultra-high flow stress ranging from 600 to 800 MPa accompanied with a prominent plastic deformability. In contrast, a relatively lower flow stress with limited ductility was observed in tension tests at room temperature. The asymmetry in tension-compression behaviors may arise from different deformation mechanisms. Without the confinement effect imposed by compressive stress, co-deformation mediated by dislocations and stacking faults in the intermetallics is hard to activate [32]. Instead, as a consequence of stress concentration, the delamination of intermetallic-Al interface would lead to pre-mature fracture in tension. Once rosettes fail, the soft matrix undergoes a surge of stress and fails afterwards. This hypothesis is evidenced by the fracture surface morphology. As is shown in Fig. 8, Al-rich matrix forms ridges around intermetallic rosettes, indicating its predominant role in carrying plastic flow while rosettes reveal cleavage fractures.

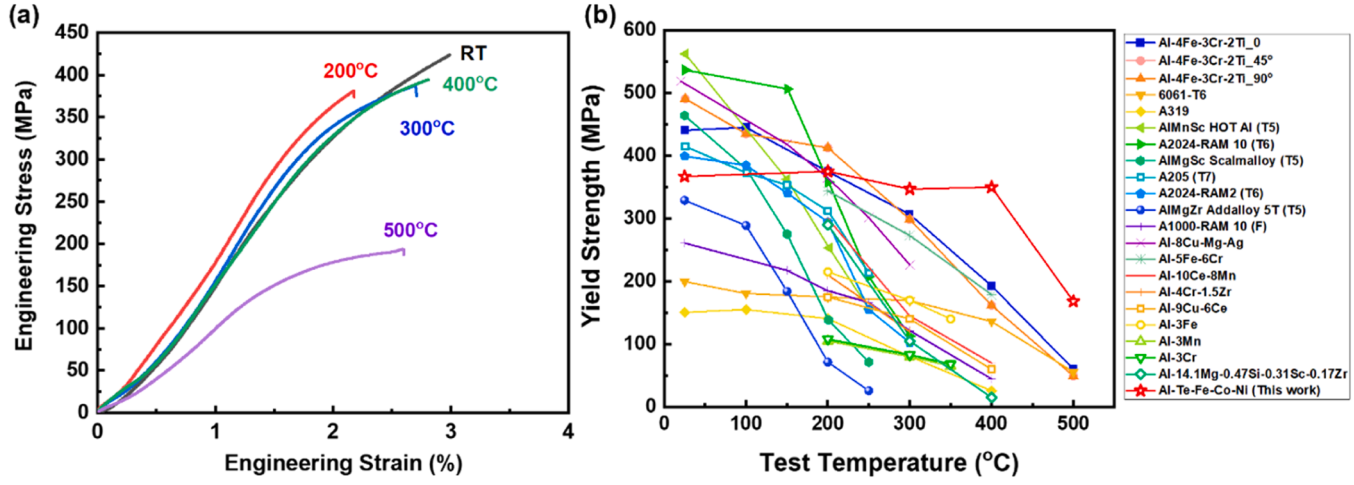

Fig. 7. (a) In-situ tensile stress-strain curves for the as-printed specimens tested at room and elevated temperatures. (b) A literature survey on the relationship of yield stresses and test temperatures for selected cast or LPBF-processed Al alloys, including Al-4Fe-3Cr-2Ti [42], AA 6061 (T6) [43], A319 [44], AlMnSc HOT Al [45], A2024-RAM10 (T6) [46], AlMgSc Scalmalloy (T5) [47], A205 (T7) [48], A2024-RAM2 (T6) [46], AlMgZr Addalloy 5T (T5) [49,50], A1000-RAM 10 (F) [46], Al-8Cu-Mg-Ag [51], Al-5Fe-6Cr [52], Al-10Ce-8Mn [25], Al-4Cr-1.5Zr [53], Al-9Cu-6Ce [54], Al-3Fe [15], Al-3Mn [15], Al-3Cr [15], Al-Mg-Si-Sc-Zr [55].

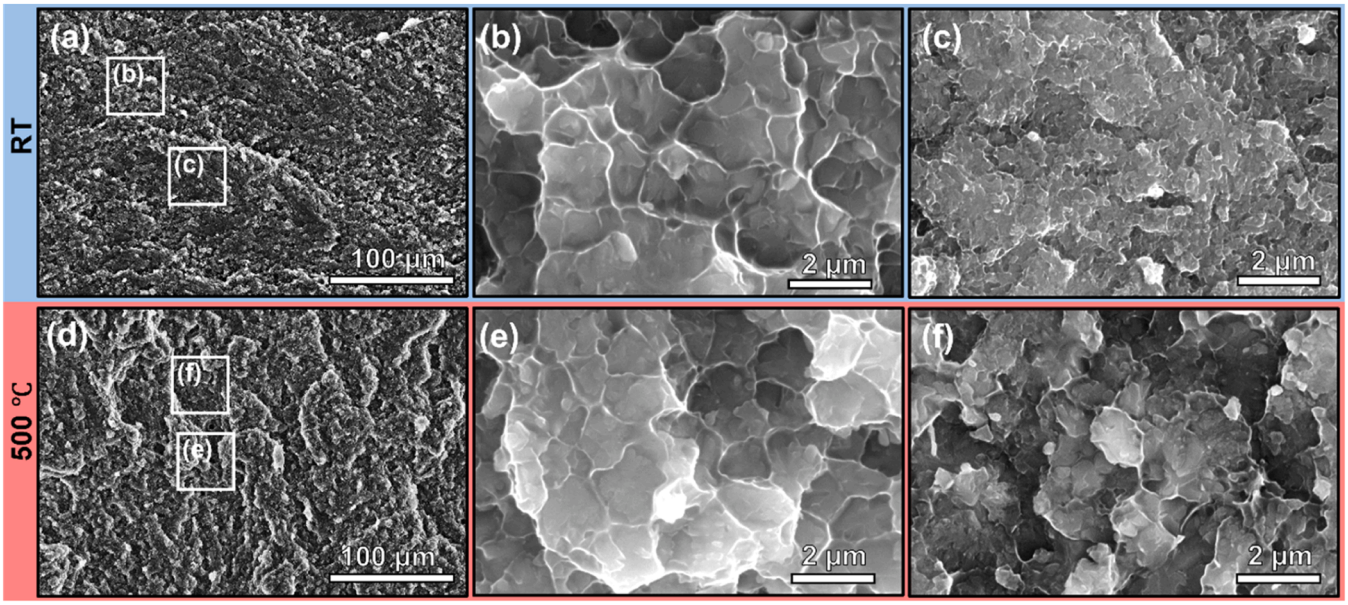

Fig. 8. SEM micrographs showing the fracture surface for the AM Al alloys tested at (a-c) room temperature and (d-f) 500 °C. (b) and (e) capture the fractured regions with coarse rosettes, while (c) and (f) reveal the fractured fine rosettes at each test temperature.

4. Conclusions

In summary, this study presented a custom-design high-strength heterogeneous Al-2Ti-2Fe-2Co-2Ni (at%) Al alloy containing interesting intermetallic rosettes fabricated by laser powder bed fusion. With the validated thermal and microstructural stability, the current alloy shows a high strength among a wide temperature range, which sheds lights on the development of high-strength, deformable Al alloys at elevated operation temperatures.

CRediT authorship contribution statement

Anyu Shang: Writing – review & editing, Writing – original draft, Visualization, Validation, Methodology, Investigation, Formal analysis, Data curation, Conceptualization. **Benjamin Stegman:** Investigation. **Xuanyu Sheng:** Data curation. **Ke Xu:** Data curation. **Yifan Zhang:** Investigation. **Chao Shen:** Data curation. **Emiliano Flores:** Data curation. **Tanner McElroy:** Data curation. **Haiyan Wang:** Supervision, Software, Resources, Project administration, Funding acquisition. **Xinghang Zhang:** Writing – review & editing, Supervision, Software, Resources, Project administration, Funding acquisition, Conceptualization.

Declaration of competing interest

The authors declare that they have no known competing financial interests or personal relationships that could have appeared to influence the work reported in this paper.

Data availability

Data will be made available on request.

Acknowledgements

This work was supported primarily by NSF-DMR-MMN 2210152. Access to the Electron Microscopy Facility center at Purdue University is also acknowledged. We also acknowledge the DURIP funding N00014-20-1-2659 for the usage of high temperature in situ tension stage. We also acknowledge technical assistance on TEM experiment from Mr. Huan Li.

Supplementary materials

Supplementary material associated with this article can be found, in the online version, at doi:10.1016/j.addlet.2024.100234.

References

[1] C. Galy, E. Le Guen, E. Lacoste, C. Arvieu, Main defects observed in aluminum alloy parts produced by SLM: from causes to consequences, Addit. Manuf. 22 (2018) 165–175, https://doi.org/10.1016/j.addma.2018.05.005.
[2] F.M. Ghaini, M. Sheikhi, M.J. Torkamany, J. Sabbaghzadeh, The relation between liquation and solidification cracks in pulsed laser welding of 2024 aluminium alloy, Mater. Sci. Eng.: A 519 (2009) 167–171, https://doi.org/10.1016/j.msea.2009.04.056.
[3] W. Stopyra, K. Gruber, I. Smolina, T. Kurzynowski, B. Kuźnicka, Laser powder bed fusion of AA7075 alloy: influence of process parameters on porosity and hot cracking, Addit. Manuf. 35 (2020) 101270, https://doi.org/10.1016/j.addma.2020.101270.
[4] Y. Cao, H.L. Wei, T. Yang, T.T. Liu, W.H. Liao, Printability assessment with porosity and solidification cracking susceptibilities for a high strength aluminum alloy during laser powder bed fusion, Addit. Manuf. 46 (2021) 102103, https://doi.org/10.1016/j.addma.2021.102103.
[5] H.R. Kotadia, G. Gibbons, A. Das, P.D. Howes, A review of laser powder bed fusion additive manufacturing of aluminium alloys: microstructure and properties, Addit. Manuf. 46 (2021) 102155, https://doi.org/10.1016/j.addma.2021.102155.
[6] Q. Tan, J. Zhang, Q. Sun, Z. Fan, G. Li, Y. Yin, Y. Liu, M.-X. Zhang, Inoculation treatment of an additively manufactured 2024 aluminium alloy with titanium nanoparticles, Acta Mater. 196 (2020) 1–16, https://doi.org/10.1016/j.actamat.2020.06.026.
[7] I.M. Kusoglu, B. Gökce, S. Barcikowski, Research trends in laser powder bed fusion of Al alloys within the last decade, Addit. Manuf. 36 (2020) 101489, https://doi.org/10.1016/j.addma.2020.101489.
[8] N.T. Aboulkhair, M. Simonelli, L. Parry, I. Ashcroft, C. Tuck, R. Hague, 3D printing of Aluminium alloys: additive Manufacturing of Aluminium alloys using selective laser melting, Prog. Mater. Sci. 106 (2019) 100578, https://doi.org/10.1016/j.pmatsci.2019.100578.
[9] I. Polmear, D. St John, J.-F. Nie, M. Qian, Light alloys: Metallurgy of the Light Metals, Elsevier/Butterworth-Heinemann, 2017. https://espace.library.uq.edu.au/view/UQ:687429. accessed January 23, 2024.
[10] R.A. Michi, A. Plotkowski, A. Shyam, R.R. Dehoff, S.S. Babu, Towards high-temperature applications of aluminium alloys enabled by additive manufacturing, Int. Mater. Rev. 67 (2022) 298–345, https://doi.org/10.1080/09506608.2021.1951580.
[11] H.B. Henderson, J.A. Hammons, A.A. Baker, S.K. McCall, T.T. Li, A. Perron, Z. C. Sims, R.T. Ott, F. Meng, M.J. Thompson, D. Weiss, O. Rios, Enhanced thermal coarsening resistance in a nanostructured aluminum-cerium alloy produced by

additive manufacturing, Mater. Des. 209 (2021) 109988, https://doi.org/10.1016/j.matdes.2021.109988.
[12] X. Wang, R.G. Guan, R.D.K. Misra, Y. Wang, H.C. Li, Y.Q. Shang, The mechanistic contribution of nanosized Al3Fe phase on the mechanical properties of Al-Fe alloy, Mater. Sci. Eng.: A 724 (2018) 452–460, https://doi.org/10.1016/j.msea.2018.04.002.
[13] W. Wang, N. Takata, A. Suzuki, M. Kobashi, M. Kato, High-temperature strength sustained by nano-sized eutectic structure of Al–Fe alloy manufactured by laser powder bed fusion, Mater. Sci. Eng.: A 838 (2022) 142782, https://doi.org/10.1016/j.msea.2022.142782.
[14] X. Qi, N. Takata, A. Suzuki, M. Kobashi, M. Kato, Managing both high strength and thermal conductivity of a laser powder bed fused Al–2.5Fe binary alloy: effect of annealing on microstructure, Mater. Sci. Eng.: A (2020) 140591, https://doi.org/10.1016/j.msea.2020.140591.
[15] T. Kimura, T. Nakamoto, T. Ozaki, T. Miki, Microstructures and mechanical properties of aluminum-transition metal binary alloys (Al-Fe, Al-Mn, and Al-Cr) processed by laser powder bed fusion, J. Alloy. Compd. 872 (2021) 159680, https://doi.org/10.1016/j.jallcom.2021.159680.
[16] J. Deng, C. Chen, X. Liu, Y. Li, K. Zhou, S. Guo, A high-strength heat-resistant Al−5.7Ni eutectic alloy with spherical Al3Ni nano-particles by selective laser melting, Scr. Mater. 203 (2021) 114034, https://doi.org/10.1016/j.scriptamat.2021.114034.
[17] I.S. Loginova, M.V. Sazerat, P.A. Loginov, A.V. Pozdniakov, N.A. Popov, A. N. Solonin, Evaluation of microstructure and hardness of novel Al-Fe-Ni alloys with high thermal stability for laser additive manufacturing, JOM 72 (2020) 3744–3752, https://doi.org/10.1007/s11837-020-04321-2.
[18] H. Ding, Y. Xiao, Z. Bian, Y. Wu, H. Yang, H. Wang, Design, microstructure and thermal stability of a novel heat-resistant Al-Fe-Ni alloy manufactured by selective laser melting, J. Alloy. Compd. 885 (2021) 160949, https://doi.org/10.1016/j.jallcom.2021.160949.
[19] J.L. Lu, X. Lin, H.L. Liao, N. Kang, W.D. Huang, C. Coddet, Compression behaviour of quasicrystal/Al composite with powder mixture driven layered microstructure prepared by selective laser melting, Opt. Laser Technol. 129 (2020) 106277, https://doi.org/10.1016/j.optlastec.2020.106277.
[20] A.P.M. de Araujo, S. Pauly, R.L. Batalha, F.G. Coury, C.S. Kiminami, V. Uhlenwinkel, P. Gargarella, Additive manufacturing of a quasicrystal-forming Al95Fe2Cr2Ti1 alloy with remarkable high-temperature strength and ductility, Addit. Manuf. 41 (2021) 101960, https://doi.org/10.1016/j.addma.2021.101960.
[21] G. Liu, S. Wang, A. Misra, J. Wang, Interface-mediated plasticity of nanoscale Al–Al2Cu eutectics, Acta Mater. 186 (2020) 443–453, https://doi.org/10.1016/j.actamat.2020.01.024.
[22] S.J. Wang, G. Liu, D.Y. Xie, Q. Lei, B.P. Ramakrishnan, J. Mazumder, J. Wang, A. Misra, Plasticity of laser-processed nanoscale AlAl2Cu eutectic alloy, Acta Mater. 156 (2018) 52–63, https://doi.org/10.1016/j.actamat.2018.06.038.
[23] K. Sisco, A. Plotkowski, Y. Yang, D. Leonard, B. Stump, P. Nandwana, R.R. Dehoff, S.S. Babu, Microstructure and properties of additively manufactured Al–Ce–Mg alloys, Sci. Rep. 11 (2021) 6953, https://doi.org/10.1038/s41598-021-86370-4.
[24] H. Hyer, A. Mehta, K. Graydon, N. Kljestan, M. Knezevic, D. Weiss, B. McWilliams, K. Cho, Y. Sohn, High strength aluminum-cerium alloy processed by laser powder bed fusion, Addit. Manuf. 52 (2022) 102657, https://doi.org/10.1016/j.addma.2022.102657.
[25] A. Plotkowski, K. Sisco, S. Bahl, A. Shyam, Y. Yang, L. Allard, P. Nandwana, A. M. Rossy, R.R. Dehoff, Microstructure and properties of a high temperature Al–Ce–Mn alloy produced by additive manufacturing, Acta Mater. 196 (2020) 595–608, https://doi.org/10.1016/j.actamat.2020.07.014.
[26] C.N. Ekaputra, D. Weiss, J.-E. Mogonye, D.C. Dunand, Eutectic, precipitation-strengthened alloy via laser fusion of blends of Al-7Ce-10Mg (wt.%), Zr, and Sc powders, Acta Mater. 246 (2023) 118676, https://doi.org/10.1016/j.actamat.2023.118676.
[27] J.A. Glerum, C. Kenel, T. Sun, D.C. Dunand, Synthesis of precipitation-strengthened Al-Sc, Al-Zr and Al-Sc-Zr alloys via selective laser melting of elemental powder blends, Addit. Manuf. 36 (2020) 101461, https://doi.org/10.1016/j.addma.2020.101461.
[28] J.H. Martin, B.D. Yahata, J.M. Hundley, J.A. Mayer, T.A. Schaedler, T.M. Pollock, 3D printing of high-strength aluminium alloys, Nature 549 (2017) 365–369, https://doi.org/10.1038/nature23894.
[29] Y. Li, H. Li, L. Katgerman, Q. Du, J. Zhang, L. Zhuang, Recent advances in hot tearing during casting of aluminium alloys, Prog. Mater. Sci. 117 (2021) 100741, https://doi.org/10.1016/j.pmatsci.2020.100741.
[30] D.G. Eskin, L.K. Suyitno, Mechanical properties in the semi-solid state and hot tearing of aluminium alloys, Prog. Mater. Sci. 49 (2004) 629–711, https://doi.org/10.1016/S0079-6425(03)00037-9.
[31] S. Kou, A criterion for cracking during solidification, Acta Mater. 88 (2015) 366–374, https://doi.org/10.1016/j.actamat.2015.01.034.
[32] A. Shang, B. Stegman, K. Choy, T. Niu, C. Shen, Z. Shang, X. Sheng, J. Lopez, L. Hoppenrath, B.P. Zhang, H. Wang, P. Bellon, X. Zhang, Additive manufacturing of an ultrastrong, deformable Al alloy with nanoscale intermetallics, Nat. Commun. 15 (2024) 5122, https://doi.org/10.1038/s41467-024-48693-4.
[33] A. Shang, B. Stegman, D. Sinclair, X. Sheng, L. Hoppenrath, C. Shen, K. Xu, E. Flores, H. Wang, N. Chawla, X. Zhang, Crack mitigation strategies for a high-strength Al alloy Al92Ti2Fe2Co2Ni2 fabricated by additive manufacturing, J. Mater. Res. Technol. 30 (2024) 5497–5511, https://doi.org/10.1016/j.jmrt.2024.04.191.
[34] Y.L. Tian, R.W. Kraft, Mechanisms of Pearlite Spheroidization, Metall. Trans. A 18 (1987) 1403–1414, https://doi.org/10.1007/BF02646654.
[35] Mechanisms of pearlite spheroidization: insights from 3D phase-field simulations, Acta Mater. 161 (2018) 400–411, https://doi.org/10.1016/j.actamat.2018.09.043.
[36] E.A. Marquis, D.N. Seidman, Nanoscale structural evolution of Al3Sc precipitates in Al(Sc) alloys, Acta Mater. 49 (2001) 1909–1919, https://doi.org/10.1016/S1359-6454(01)00116-1.
[37] Z. Bian, S. Dai, L. Wu, Z. Chen, M. Wang, D. Chen, H. Wang, Thermal stability of Al–Fe–Ni alloy at high temperatures, J. Mater. Res. Technol. 8 (2019) 2538–2548, https://doi.org/10.1016/j.jmrt.2019.01.028.
[38] H. Ding, Y. Xiao, Z. Bian, Y. Wu, H. Yang, Y. Li, Z. Chen, H. Wang, H. Wang, Effect of in-situ TiB2 particles on microstructure and mechanical properties of Al–Fe–Ni manufactured by selective laser melting, Mater. Sci. Eng.: A 845 (2022) 143065, https://doi.org/10.1016/j.msea.2022.143065.
[39] M. Mantina, S.L. Shang, Y. Wang, L.Q. Chen, Z.K. Liu, 3 d transition metal impurities in aluminum: a first-principles study, Phys. Rev. B 80 (2009) 184111, https://doi.org/10.1103/PhysRevB.80.184111.
[40] Y.F. Zhang, R. Su, D.Y. Xie, T.J. Niu, S. Xue, Q. Li, Z. Shang, J. Ding, N.A. Richter, J. Wang, H. Wang, X. Zhang, Design of super-strong and thermally stable nanotwinned Al alloys *via* solute synergy, Nanoscale 12 (2020) 20491–20505, https://doi.org/10.1039/D0NR05707J.
[41] N.A. Richter, Y.F. Zhang, M. Gong, T. Niu, B. Yang, S. Xue, J. Wang, H. Wang, X. Zhang, Solute synergy induced thermal stability of high-strength nanotwinned Al-Co-Zr alloys, Mater. Sci. Eng.: A 862 (2023) 144477, https://doi.org/10.1016/j.msea.2022.144477.
[42] A.P.M. de Araujo, C.S. Kiminami, V. Uhlenwinkel, P. Gargarella, High-temperature tensile properties of an aluminum quasicrystal-forming alloy manufactured by laser powder bed fusion, Mater. Sci. Eng.: A (2023) 145670, https://doi.org/10.1016/j.msea.2023.145670.
[43] M.-N. Su, B. Young, Material properties of normal and high strength aluminium alloys at elevated temperatures, Thin-Wall. Struct. 137 (2019) 463–471, https://doi.org/10.1016/j.tws.2019.01.012.
[44] E. Rincon, H.F. Lopez, M.M. Cisneros, H. Mancha, Temperature effects on the tensile properties of cast and heat treated aluminum alloy A319, Mater. Sci. Eng.: A 519 (2009) 128–140, https://doi.org/10.1016/j.msea.2009.05.022.
[45] F. B., Developing a High Operating Temperature Al Alloy for AM: Amaero H.O.T. Al, Developing a High Operating Temperature Al Alloy for AM: Amaero H.O.T. Al, (2021). Developing a High Operating Temperature Al Alloy for AM: Amaero H.O.T. Al.
[46] 3d Printed Aluminum - AM Powder Solution - 3d Printing Industry, Elementum3d (2021). https://www.elementum3d.com/aluminum/(accessed April 19, 2024).
[47] Scalmalloy, Apworks (2024). https://www.apworks.de/scalmalloy (accessed April 19, 2024).
[48] A20X™ ALLOY FOR AEROSPACE | Eckart Germany, A20X™ ALLOY FOR AEROSPACE | Eckart Germany (2024). https://eckart.net/de/en/am/a20x (accessed April 19, 2024).
[49] B. J., Addalloy® 5T: 3D Printing Aluminum with High Strength and Ductility - Review of Published Research, 2020.
[50] Addalloy® 5T Powder, NanoAL (2024). https://www.nanoal.com/addalloy-5t-powder (accessed April 19, 2024).
[51] D.H. Xiao, J.N. Wang, D.Y. Ding, S.P. Chen, Effect of Cu content on the mechanical properties of an Al–Cu–Mg–Ag alloy, J. Alloy. Compd. 343 (2002) 77–81, https://doi.org/10.1016/S0925-8388(02)00076-2.
[52] M.T. Pérez-Prado, A. Martin, D.F. Shi, S. Milenkovic, C.M. Cepeda-Jiménez, An Al-5Fe-6Cr alloy with outstanding high temperature mechanical behavior by laser powder bed fusion, Addit. Manuf. 55 (2022) 102828, https://doi.org/10.1016/j.addma.2022.102828.
[53] T. Kimura, T. Nakamoto, T. Ozaki, T. Miki, I. Murakami, Y. Hashizume, A. Tanaka, Microstructural development and aging behavior of Al–Cr–Zr heat-resistant alloy fabricated using laser powder bed fusion, J. Mater. Res. Technol. 15 (2021) 4193–4207, https://doi.org/10.1016/j.jmrt.2021.10.027.
[54] D.R. Manca, A.Yu. Churyumov, A.V. Pozdniakov, A.S. Prosviryakov, D.K. Ryabov, A.Yu. Krokhin, V.A. Korolev, D.K. Daubarayte, Microstructure and properties of novel heat resistant Al–Ce–Cu alloy for additive manufacturing, Met. Mater. Int. 25 (2019) 633–640, https://doi.org/10.1007/s12540-018-00211-0.
[55] J. Bi, Z. Lei, Y. Chen, X. Chen, Z. Tian, N. Lu, X. Qin, J. Liang, Microstructure, tensile properties and thermal stability of AlMgSiScZr alloy printed by laser powder bed fusion, J. Mater. Sci. Technol. 69 (2021) 200–211, https://doi.org/10.1016/j.jmst.2020.08.033.